Significance of developmental meningeal lymphatic dysfunction in experimental post-traumatic injury

Anaïs Virenque, Hennariikka Koivisto, Salli Antila, Emma Zub, Erin Jane Rooney, Diana Miszczuk, Adrian Müller, Enija Stoka, Nicola Marchi, Kari Alitalo, et al.

Brain, Behavior, & Immunity - Health 23 (2022) 100466

Contents lists available at ScienceDirect

Brain, Behavior, & Immunity - Health

journal homepage: www.editorialmanager.com/bbih/default.aspx

Significance of developmental meningeal lymphatic dysfunction in experimental post-traumatic injury

Anaïs Virenque [a,1], Hennariikka Koivisto [b,1], Salli Antila [c], Emma Zub [d], Erin Jane Rooney [a], Diana Miszczuk [b], Adrian Müller [b], Enija Stoka [a], Nicola Marchi [d], Kari Alitalo [c], Heikki Tanila [b], Francesco Mattia Noe [a,b,*]

[a] Neuroscience Center, Helsinki Institute of Life Science (HiLIFE), University of Helsinki, 00290, Helsinki, Finland
[b] A.I. Virtanen Institute for Molecular Sciences, University of Eastern Finland, 70210, Kuopio, Finland
[c] Wihuri Research Institute and Translational Cancer Medicine Program, Biomedicum Helsinki, University of Helsinki, 00290, Helsinki, Finland
[d] Cerebrovascular and Glia Research, Institute of Functional Genomics, University of Montpellier, CNRS, INSERM, Montpellier, France

ARTICLE INFO

Keywords:
Meningeal lymphatic vessels
Chronic traumatic brain injury
Behavioral dysfunctions
Neuroinflammation
Cortical lesion development

ABSTRACT

Understanding the pathological mechanisms unfolding after chronic traumatic brain injury (TBI) could reveal new therapeutic entry points. During the post-TBI sequel, the involvement of cerebrospinal fluid drainage through the meningeal lymphatic vessels was proposed. Here, we used K14-VEGFR3-Ig transgenic mice to analyze whether a developmental dysfunction of meningeal lymphatic vessels modifies post-TBI pathology. To this end, a moderate TBI was delivered by controlled cortical injury over the temporal lobe in male transgenic mice or their littermate controls. We performed MRI and a battery of behavioral tests over time to define the post-TBI trajectories. In vivo analyses were integrated by ex-vivo quantitative and morphometric examinations of the cortical lesion and glial cells.

In post-TBI K14-VEGFR3-Ig mice, the recovery from motor deficits was protracted compared to littermates. This outcome is coherent with the observed slower hematoma clearance in transgenic mice during the first two weeks post-TBI. No other genotype-related behavioral differences were observed, and the volume of cortical lesions imaged by MRI *in vivo*, and confirmed by histology ex-vivo, were comparable in both groups. However, at the cellular level, post-TBI K14-VEGFR3-Ig mice exhibited an increased percentage of activated Iba1 microglia in the hippocampus and auditory cortex, areas that are proximal to the lesion.

Although not impacting or modifying the structural brain damage and post-TBI behavior, a pre-existing dysfunction of meningeal lymphatic vessels is associated with morphological microglial activation over time, possibly representing a sub-clinical pathological imprint or a vulnerability factor. Our findings suggest that pre-existing mLV deficits could represent a possible risk factor for the overall outcome of TBI pathology.

1. Introduction

Traumatic brain injury (TBI) leads to lifetime pathologies, including the development of neurocognitive and motor dysfunctions, and psychiatric comorbidities (Frieden, Houry, Baldwin), representing one of the leading causes of disability worldwide.

Longitudinal studies demonstrated that the development of TBI-related dysfunctions is a dynamic process (McMillan et al., 2012), suggesting a secondary progressive disease. Persistent neurodegenerative, neuroinflammatory, and cerebrovascular events (Janigro et al., 2021; Owens et al., 2021; Ichkova et al., 2020; Giannoni et al., 2018) can underlie the progression of brain damage (Corps et al., 2015) and the occurrence of neurological dysfunctions (Owens et al., 2021; Mouzon et al., 2014; Holmin et al., 1998; Noé and Marchi, 2019). However, the pathophysiological mechanisms sustaining the development of a chronic pathology remain a matter of intense scrutiny.

Meningeal lymphatic vessels (mLVs) (Aspelund et al., 2015; Louveau et al., 2015) may play a role in the pathophysiology of

Abbreviations: TBI, Traumatic Brain Injury; mLV, Meningeal Lymphatic Vessel; CCI, Controlled Cortical Injury.

* Corresponding author. HiLIFE, Neuroscience Center, Helsinki University, Helsinki, Finland.
E-mail address: francesco.noe@helsinki.fi (F.M. Noe).

[1] Both Authors equally contributed to the manuscript.

https://doi.org/10.1016/j.bbih.2022.100466
Received 13 January 2022; Received in revised form 24 April 2022; Accepted 26 April 2022
Available online 4 May 2022

neurodegenerative diseases (Noé and Marchi, 2019; Hu et al., 2020; Song et al., 2020; Chen et al., 2020; Tsai et al., 2022; Yanev et al., 2020; Louveau et al., 2018; das Neves et al., 2021): mLVs are critical for the drainage of cerebral fluids, as well as for the clearance of macromolecules and immune cells from the brain (Louveau et al., 2018; Ahn et al., 2019); their disruption can promote the accumulation of neurotoxic molecules in the brain (Da Mesquita et al., 2018a; Patel et al., 2019). Increased parenchyma accumulation of tau and albumin, and amyloid deposition in the meninges, have been reported in murine models presenting functional deficit in the meningeal lymphatic system (Patel et al., 2019; Da Mesquita et al., 2018b; Ding et al., 2021; Zou et al., 2019). This evidence supports the hypothesis that mLV alterations can affect the severity of the cognitive decline in Alzheimer's disease (Patel et al., 2019; Da Mesquita et al., 2018b) and the pathophysiology of Parkinson's disease (Ding et al., 2021; Zou et al., 2019). An involvement of mLV drainage has also been proposed in the pathophysiology of ischemic and hemorrhagic stroke (Chen et al., 2020; Tsai et al., 2022; Yanev et al., 2020), substantiating the importance of these lymphatic vessels in multiple neurological indications.

Meningeal lymphatic dysfunctions also affect the neuro-inflammatory or neuro-immune response (Noé and Marchi, 2019; Wojciechowski et al., 2021). In this respect, mLVs could have a role in the pathophysiology of TBI (Bolte et al., 2020): pharmacological suppression of lymphatic function before TBI exacerbates neuroinflammation and cognitive dysfunction in the acute phases of the pathology (Bolte et al., 2020). Understanding the impact of prolonged mLV dysfunction could reveal new therapeutic targets.

Here, we tested the hypothesis that a pre-existing congenital deficit in the meningeal lymphatic drainage could negatively modify the post-TBI sequel. To this end, we used a transgenic mouse model (the K14-VEGFR3-Ig transgenic mice) that expresses a soluble form of vascular endothelial growth factor receptor 3, lacks mLVs, and has congenital-onset lymphedema (Mäkinen et al., 2001). For up to two months, we tracked the behavioral, brain structural, and cellular pathological modifications during the acute and the early chronic phases post-TBI.

2. Material and methods

Mice: Adult male (5 months old) C57BL/6JOlaHsd (WT) or littermate K14-VEGFR3-Ig mice (on C57BL/6JOlaHsd background; TG) (Mäkinen et al., 2001) were used in this study. Mixed WT and TG mice were housed in standard laboratory cages (four animals per cage, until surgery) in a controlled enriched environment (constant temperature, 22 ± 1 °C, humidity 50–60%, lights on 07:00–19:00), with food and water available ad libitum. After TBI induction, mice were kept two per cage, separated by a pierced partition. Initial breeding pairs of K14-VEGFR3-Ig mice were provided by Prof. K. Alitalo (University of Helsinki), and the colony has been further expanded and maintained at the University of Eastern Finland. Genotype screening was routinely confirmed by polymerase chain reaction analysis of ear punch samples. All animal procedures were performed following the guidelines of the European Community Council Directives 2010/63/EU and approved by the Animal Experiment Board of Finland (ESAVI/8787).

Controlled cortical injury (CCI) mouse model of TBI: All surgical procedures were performed aseptically whenever possible. The CCI protocol used for this study has been described in detail previously (Wojciechowski et al., 2021). Briefly, each mouse was deeply anesthetized with isoflurane in air (0.5–1% for maintenance anesthesia), the head fixed to a stereotaxic frame (Kopf, USA) and, after skull exposure, a 5 mm circular craniotomy was manually drilled over the left parieto-temporal cortex (craniotomy posterior edge opposed to the lambdoid suture and right edge to the sagittal suture). The carved bone was carefully removed, without disrupting the underlying dura, and placed in 1% povidone-iodide solution. To induce CCI, a 3 mm impact probe (blunt tip) was connected to an electromagnetic impact actuator (ImpactOne, Leica, USA), and positioned to the center of the exposed dura perpendicular to the brain surface. The animal was disconnected from isoflurane anesthesia for 5 min, and CCI was delivered at a strike depth of 0.5 mm, a speed of 5.0 m/s, and a dwell time of 100 ms. The total duration of the craniotomy procedure including anesthesia induction was 35–40 min. After the impact, the mouse was reconnected to the isoflurane system, and the removed skull returned to its original position and secured with bone cement (Selectaplus + Palacos R + G 50/50, Heraeus Medical, Germany). The scalp was sutured (total duration of post-impact surgery: 10 min), and treated with Cicatrene powder (Neomycin + Bacitracin; Johnson & Johnson, Italy) and Terramycin spray (Oxytetracycline; Zoetis, Finland). As post-surgical care, the mouse was injected i.p. with 1 mL pre-warmed sterile saline (35 °C) and allowed to fully recover in an incubator at 32 °C. Similar parameters were used to induce CCI in both WT and TG animals, which resulted in a moderate injury with no mortality. Sham-operated control animals (SHAMs) underwent the same surgical procedures including craniotomy, bone removal and 5 min discontinuation of isoflurane anesthesia, but no impact was delivered. After the 5 min withdrawal of anesthesia the bone was replaced and cemented and the skin sutured as described above. Anesthesia parameters and duration was comparable in SHAM and CCI mice.

Analysis of cortical-dependent sensory-motor functions: An extensive description of the methodologies is available in the supplementary data. Behavioral characterization studies were conducted on two independent cohorts, both including n = 6 mice in each experimental group (*i.e.*, WT-SHAM, WT-CCI; TG-SHAM and TG-CCI). A total of n = 12 mice/experimental group were prepared for behavioral analyses. Littermate mice were randomized within the experimental groups. All animals underwent a battery of behavioral tests, covering the acute and early chronic phases of TBI pathology (2 months after injury). Briefly, to assess motor deficits and recovery after TBI we used the *inclined angle board test* (a simplified version of the Composite Neuroscore paradigm) at 2, 7, and 10 days post-injury (dpi) and compared the outcome to the pre-injury baseline results (assessed 5 days before CCI induction). Sensorimotor gating (acoustic startle + pre-pulse inhibition), gait pattern (Catwalk), and motor coordination and balance (Rotarod) were tested respectively during the 3rd, 4th, and 5th-week post-CCI. To assess spontaneous activity and anxiety, mice performed the open-field test (OF, on the 3rd-week post-CCI). Spatial learning and memory were assessed with the Morris swim task on the 6th-week post-CCI, and the passive avoidance test was used to assess long-term fear-associated memory (on the 8th-week post-CCI). The order of the tests (inclined angle board, OF, acoustic startle, catwalk, rotarod, Morris swim task, and passive avoidance; Fig. 2A) was chosen to take into account the stress level associated with each test. Seven mice were excluded from the behavioral tests due to surgical problems (*i.e.*, damage to the dura during craniotomy or failure of the impactor in delivering the trauma), or evidence of motor seizures in the 24 h following TBI induction. A total of n = 10 (WT-SHAM); n = 10 (WT-CCI); n = 11 (TG-SHAM) and n = 10 (TG-CCI) have been used for the final statistical analyses.

At the beginning of the experiment, all animals underwent acclimation to handling and testing environment. Behavioral tests were performed in a dimly lit, soundproof room with a familiar environment, and the person performing the tests was blinded as to the treatment of the mice. Each test was carried out during the light phase of the light/dark cycle. A detailed description of the behavioral test parameters is provided in the Supplementary Information.

Magnetic Resonance Imaging (MRI) Procedure: MRI was performed on a separate subset of mice (n = 8/experimental group) at 1, 3, 7, 14, and 30 days post-injury (dpi), using a 7.0 T magnetic resonance scanner (Bruker PharmaScan, Germany), equipped with a mouse brain surface coil. Mice were anesthetized using 1.0% isoflurane (carrier gas: 70% N2 + 30% O2) and breath rate and body temperature were monitored during the entire acquisition time. High-resolution structural 3D MRI was acquired with a multi-gradient recalled echo (MGRE) sequence with 150 ms repetition time, flip angle = 30°; field-of-view = 12.8 mm ×

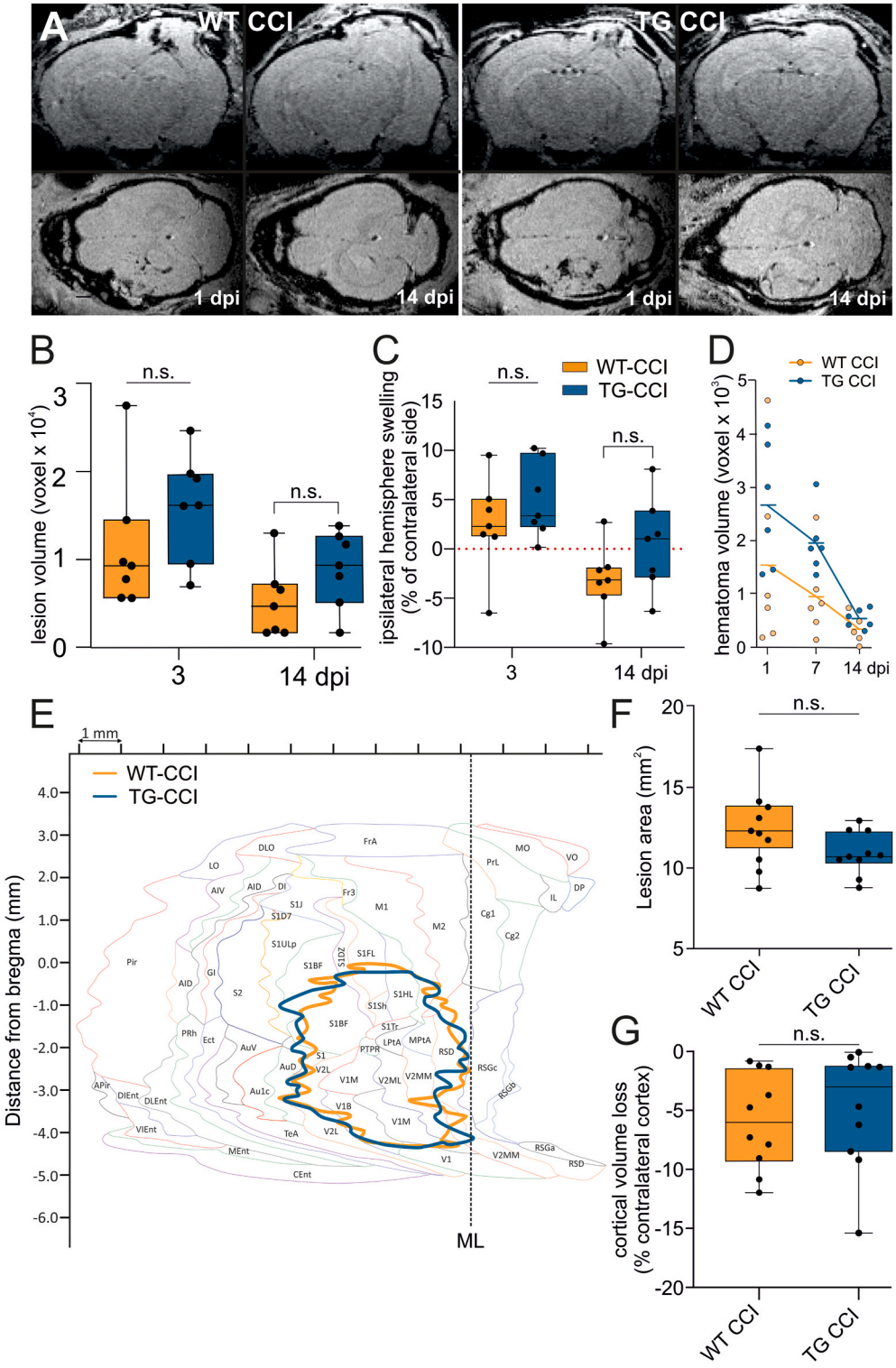

Fig. 1. Formation of cortical lesion and hematoma regression after TBI are not affected by the pre-existing mLV dysfunction. (A) Representative coronal (upper panels) and axial (lower panels) reconstructed T1-weighted MRI images showing the hemorrhage extension in WT CCI and TG CCI brains, as recorded at 1 and 14 days post-TBI induction (dpi). Hematoma is visible at 1 dpi, and mostly regress by 14 dpi, in both TG and WT mice. (B–C) *In vivo* analysis of lesion formation. Longitudinal analyses of cortical and subcortical lesion volume ipsilateral to the site of injury and edema formation (swelling) show no genotype related differences. (D) Regression of the hematoma volume in TG and WT mice, analyzed at 1, 7 and 14 days after TBI. For the definitions of the hematoma volume see the main text. (E) Unfolded cortical map showing the mean lesion extension in WT- (orange) and TG-CCI (blue) mice. In both genotypes, CCI induction resulted in a similar lesion affecting prevalently the visual and somatosensory cortices. (F–G) Post-mortem histological analyses at 2 month post-TBI show similar lesions in the two genotypes. (F) Evaluation of the cortical area affected by the brain injury (unfolded cortical map quantification). (G) Cortical volume loss as evaluated *ex vivo*. Data analyses: Kruskal Wallis test with Sidak correction. A linear mixed-effect model (lme) was applied to assess statistical differences in the analysis of hematoma volume regression. dpi: days post injury, ML: mid line. For cortical area annotation, refer to Franklin and Paxinos mouse brain atlas (Franklin and Paxinos, 2007). (For interpretation of the references to colour in this figure legend, the reader is referred to the Web version of this article.)

25.6 mm × 9.6 mm (acquisition matrix 128 × 256 x 96). Twelve echoes with echo time (TE) ranging from 3.04 ms to 47.82 ms (4.07 ms ΔTE) were collected, and all 12 echo images were summed together. This resulted in T1/T2* mixed contrast and 100 μm isotropic resolution. Aedes (http://aedes.uef.fi), an in-house MatLab (MathWorks, USA) program, with a SWI plugin was used to analyze the hematoma volume, lesion volume, and brain swelling/atrophy of previously acquired MRI data (Hayward et al., 2011; Hänninen et al., 2017). Regions of interest (ROIs; lesion, hematoma, ipsilateral hemisphere, and contralateral hemisphere) were outlined for volumetric analysis, avoiding the brain-skull interface, throughout the entire extension of the brain (excluding olfactory bulbs and cerebellum). ROIs were outlined through 80 slices on the coronal plane images and adjusted on the sagittal and transverse planes.

Hematoma volume and cerebral swelling: hemorrhagic (hematoma) and edema (cerebral swelling) signals were analyzed on T2* maps generated from the 3D MGRE data, with T2* relaxation time values included between 12 and 80 msec (dynamic range of brain tissue). The

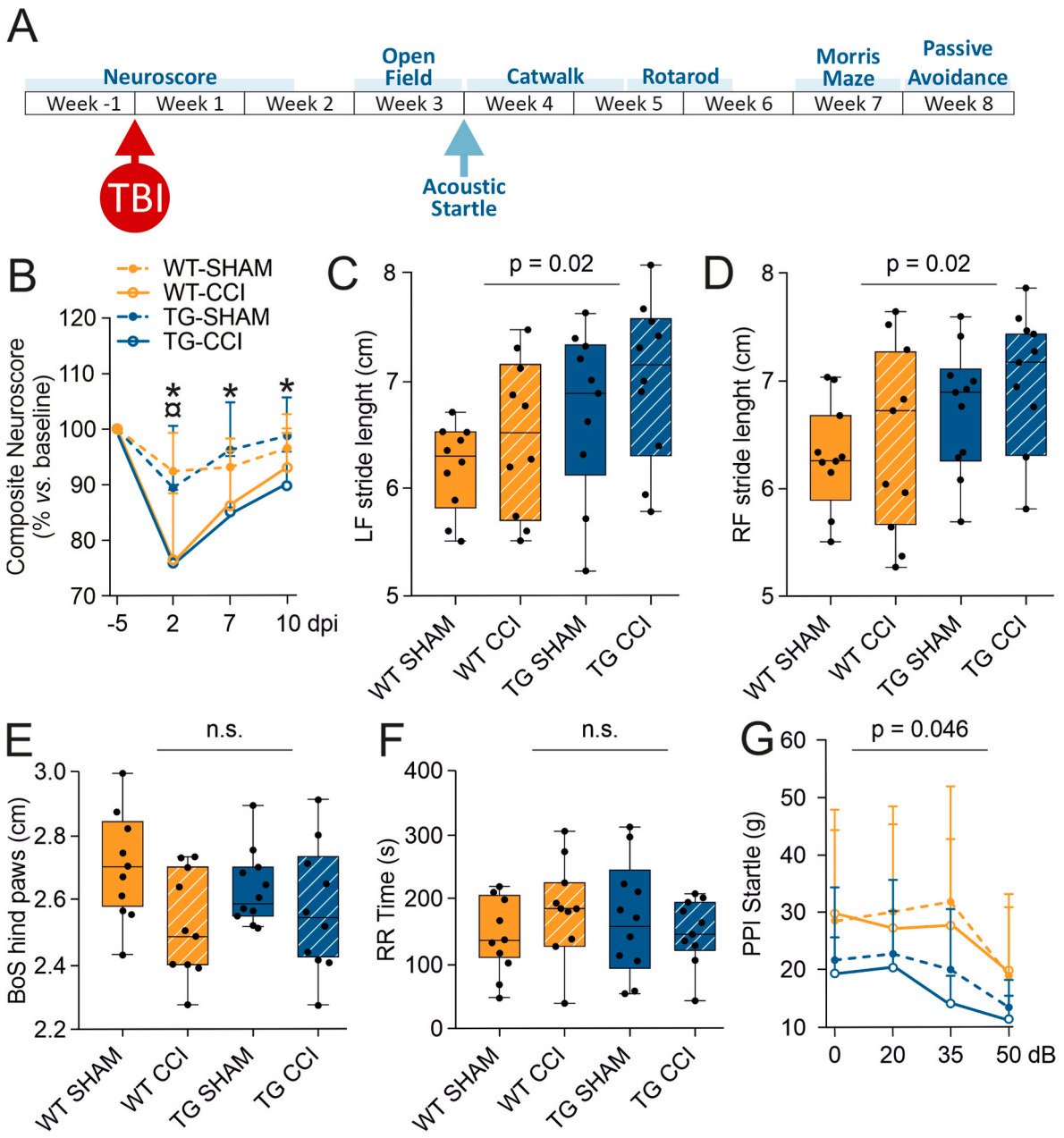

Fig. 2. Analysis of acute and subacute TBI-related functional impairments in WT-CCI and TG-CCI. CCI is characterized by a strong and transient acute impairment of motor functions, however the lack of mLVs does not affect the long-term outcome. (A) Study design of the behavioral test battery to analyze the development of neurological dysfunctions after TBI. (B) Simplified Composite Neuroscore tested at the pre-injury baseline and at 2, 7, and 10 dpi. Both TG-CCI and WT-CCI groups showed a transient impairment of motor functions after TBI. However, a prolonged deficit in the longitudinal recovery of motor functions was observed in TG-CCI mice. ¤p < 0.05 WT-CCI *vs.* WT-SHAM. *p < 0.05 TG-CCI *vs.* TG-SHAM. (C–E) Box plot illustrating the genotype effect on Catwalk-related parameters. A genotype effect is visible in the analysis of stride length, with TG mice showing a longer stride in the front paws (C,D). A TBI-related difference is present in the analysis of the base of support area (BoS) of hind paws, which is narrower in both CCI groups compared to SHAM animals (E). All the other evaluated parameters for the Catwalk gait analysis did not show differences related to the genotype or the injury. (F) No genotype or injury effect are visible from the analysis of time spent on the Rotarod. (G) Transmission of auditory sensory information to the nervous system, and associated sensorimotor processing, was assessed by pre-pulse inhibition (PPI) of startle reflex. No injury effect on sensory gating was observed. A significant genotype effect on the startle reflex was measured in TG mice, possibly due to partial hearing loss. For statistical data, see the main text and Supplementary Table 1. Data analyses: linear mixed-effect model (lme) with Sidak correction. dpi: days post injury, LP: left paw, RP: right paw, BoS: base of support area, RR: rotarod, PPI: pre-pulse inhibition. P-values are reported for the genotype effect analysis.

hematoma was defined as pixels with a T2*< 17 msec, in the cortical and subcortical regions ipsilateral to the site of injury. For the analysis of the hematoma volume, two animals were excluded (one per experimental group) because of artifacts in the T2* map on day 1.

Cerebral swelling was defined as the difference between the ipsilateral (Vi) and contralateral (Vc) hemispheres and expressed as a percentage of the contralateral hemisphere. The following formula was used:

$$\frac{Vi - Vc}{Vc} * 100$$

Lesion volume: lesion volume was defined as the cortical and subcortical regions ipsilateral to the site of injury with hyperintense signal (*i.e.*, above the mean signal of the cortical gray matter +2 standard deviation; SD).

Histological evaluation: All mice used for behavioral tests were euthanized at 60 dpi for histological and immunohistochemical analyses. Deeply anesthetized mice (overdose of ketamine + medethomidine) were transcardially perfused with ice-cold 0.9% NaCl (6 ml/min, 6 min), followed by 4% paraformaldehyde (PFA) in 0.1 M sodium phosphate buffer, pH 7.4 (6 ml/min, 15 min). Brains were dissected and post-fixed in 4% PFA by immersion for 24h at 4 °C. Thereafter, specimens were cryoprotected by incubation in 20% glycerol (in 0.02 M potassium phosphate-buffered saline – KPBS, pH 7.4) for 48 h, frozen in *N*-pentane (3 min at −60 °C), and stored at −70 °C until sectioning. Brains were sliced in 25 μm-thick coronal sections (1-in-6 series) with a sliding microtome. The first series of sections were stored in 10% formalin at RT for thionin staining. The remaining series were stored in a cryoprotectant tissue-collecting solution (30% ethylene glycol, 25% glycerol in 0.05 M sodium phosphate buffer) at −20 °C until further processing.

Quantitative and morphometric analyses of cortical lesion: For morphometric analysis, parameters of a three-dimensional lesion were determined by systematic random sampling of histological sections (1-in-6 series of 25 μm-thick thionin-stained sections, 150 μm apart from each other) throughout the mouse brain. Whole-brain section images were acquired as tiled arrays using an epifluorescence microscope (LSM 510; Zeiss, Japan) equipped with a computer-controlled stage (Cell Observer; Zeiss), aligned using the Zeiss Zen software, and uploaded into the ImageJ software (National Institutes of Health, USA) for analysis. The boundary contours of the contralateral and ipsilateral spare cortex (excluding the regions of tissue loss/cavitation and mechanically disrupted tissue at the site of injury) were manually outlined in each section. The enclosed volume within the contours was measured. The percentage of the cortical tissue corresponding to the lesion was calculated with the following formula (Zhao et al., 2018):

$$\frac{contralateral\ cortex\ volume - ipsilateral\ spare\ cortex\ volume}{contralateral\ cortex\ volume} * 100$$

No primary lesion was identified in SHAM mice, independently from the genotype.

To assess the lesion location and extent in the cerebral cortex, we used two-dimensional unfolded cortical maps generated from the thionin-stained histological sections, as previously described in detail (Ekolle Ndode-Ekane et al., 2017). The same sections acquired for the morphometric analysis were used to generate the unfolding maps of the lesioned area. Briefly, an unfolded map template was prepared based on the mouse brain atlas (Konsman, 2003), using the medial edge of the cortex and the rhinal fissure as reference points. To reveal the mediolateral location of the lesion, on each coronal section three lengths were measured using ImageJ: (L1) the length of the cortical surface from the medial reference point to the medial edge of the lesion; (L2) the surface length of the lesion; and (L3) the length from the lateral edge of the lesion to the rhinal fissure. The criterion for lesion delineation was the occurrence of neurodegeneration in layer V. Each measurement was adjusted for shrinkage by calculating the compensation ratio between each histological sections and its corresponding atlas-based template. The compensation ratio was determined by dividing the cortical surface length in the histological slice (*i.e.*, the distance from the medial reference point to the rhinal fissure) by the cortical surface length in the atlas plate, at the given anteroposterior level. The adjusted measurements from each section were then transferred to the template at the corresponding anteroposterior coordinate. Finally, the marks indicating the edges of the lesion in each successive level were connected to outline the boundaries of the lesion area. The total lesion area in the unfolded map (absolute value as mm^2) was calculated.

Morphometric and unfolded map lesion area analyses were performed by two independent observers blinded to the genotype of each animal.

Analysis of microglial activation: Microglia activation in the perilesional area was evaluated in randomly selected representative mice (n = 5/experimental group) at the time of sacrifice (60 dpi). For the immunofluorescence procedure, brain sections were washed in PBS and blocked for 1 h at RT in a solution containing 4% NGS +0,2% Triton X-100 in PBS. Sections were incubated overnight at 4 °C with the rabbit anti-Iba1 (1:500, Wako 019–19741) and the guinea pig anti-NeuN (1:500, Millipore ABN90) primary antibodies, diluted in the blocking solution. After washing in PBS, sections were incubated for 2 h at RT with Alexa Fluor 488-conjugated goat anti-rabbit and Alexa Fluor 633-conjugated goat anti guinea pig (1:250 all from Invitrogen, Thermo Fisher Scientific) secondary fluorescent antibodies in 2% NGS. Sections were washed in PBS before being mounted onto glass slides and coverslipped using Vectashield® with DAPI (BioNordika Oy). For immunochemistry analysis, we selected two areas around the lesion that presented a precise microglial activation: auditory cortex (AuD) and dorsal hippocampal formation (HPC). Three representative brain sections from each area and the corresponding contralateral side were imaged. High-resolution Z-stack images (1um each Z-plane; 15–20 μm) were captured with a confocal microscope (Zeiss LSM710), using 25X immersion objective and constant exposure settings. ZEN (Carl Zeiss GmbH) and Imaris 8.1 were used for 3D image processing. NeuN and DAPI signals were used to identify comparable areas of interest across sections and animals. Microglial morphological analysis was performed as previously described (Forner-Piquer et al., 2021). For each image, we classified microglial cells (Iba1/DAPI) based on morphology (soma size and process length), into two main subtypes: resting/ramified and activated/ameboid. For each category, cell number was measured and normalized by the total number of cells.

Statistics: All statistical analyses were run using the SPSS 25 software and confirmed by an independent researcher using R v3.5.3 software/computing environment (The R foundation for statistical computing). The specific test used for each analysis is reported in the figure legends and Table 1. Linear mixed-effects models (lme) were applied to assess statistical differences in repeated measure studies, while the univariate general linear model (GLM) was used to assess the genotype and treatment effects in the other cases. Negative binomial regression was used for modeling over-dispersed count variables. Sidak correction was used to adjust p-values in multiple comparisons. Significance was accepted at the level of $p < 0.05$. All data are presented as mean ± SD.

3. Results

Trajectories of post-TBI pathology in mice presenting a developmental mLV dysfunction. We first asked whether structural brain modifications post-TBI depend on mLV functionality. In vivo, MRI showed similar cortical lesions in post-TBI WT (WT-CCI) and K14-VEGFR3-Ig mice (TG-CCI). In both genotypes, development of post-TBI lesions were apparent at day 1 post-injury (dpi) (Fig. 1A), and the progression of the lesion volume was similar in WT-CCI (4612 ± 4429 voxels at 14 dpi) and TG-CCI mice (8542 ± 4694 voxels at 14 dpi; genotype effect: $p = 0.433$) (Fig. 1B). MRI analysis also revealed a significant reduction of swelling in the hemisphere ipsilateral to the lesion at 14 dpi (WT-CCI: 2.9 ± 1.1%, TG-CCI: 0.4 ± 4.7%) compared to 3 dpi (WT-CCI: 2.9 ± 3.8%, TG-CCI: 4.9 ± 3.9%; time effect: $p = 0.002$). No genotype-related differences were observed at either analyzed time point (3 dpi: $p = 0.57$; 14 dpi: $p = 0.23$) (Fig. 1C).

As intracerebral hematoma formation is characteristic of TBI and can impair neuronal functions, we next analyzed the resolution of the hematoma during the first two weeks after injury (Fig. 1D). Longitudinal analysis indicated a significant reduction of the hematoma over time (time effect: $p = 0.004$), which was similar in both genotypes (WT-CCI vs. TG-CCI 1 dpi: $p = 0.53$; 7 dpi: $p = 0.10$; 14 dpi: $p = 0.55$). However, we observed a trend for a slower hematoma clearance in transgenic mice (genotype effect: $p = 0.07$), suggesting an alteration in the brain clearance pathways.

Finally, ex-vivo histological analysis at 2 months post-TBI confirmed that the lesion extension is comparable in WT and TG-CCI mice. In both

Table 1
Statistical analyses of analyzed behavioural tasks.

Task	Variable	Source	df	F	Chi-Square	p-value	Mean difference	95% CI (difference)	Statistical Test	Adjustment
Neuroscore									Linear Mixed Effect Model	Bonferroni
		genotype		0,500		0,377	0,383	−2,997–3,763		
		treatment		26,625		0,001	8,793	5,413–12,174		
		genotype*treatment		4,417		0,240				
	Impairment								Univariate GLM	Bonferroni
		genotype	1	0,084		0,774	−0,201	−1,607–1,205		
		treatment	1	18,363		0,001	2,974	1,568–4,380		
		genotype*treatment	1	0,001		0,973				
		Error	37							
	Recovery								Univariate GLM	Bonferroni
		genotype	1	,0956		0,634	0,306	−0,984–1,595		
		treatment	1	42,764		0,003	2,044	0,775–3,334		
		genotype*treatment	1	11,404		0,106				
		Error	37							
Catwalk Gait	Static Data									
	Base of Support (Front paws)								Univariate GLM	Bonferroni
		genotype	1	2,760		0,105	−0,084	−0,187–0,019		
		treatment	1	0,047		0,829	−0,011	−0,114–0,092		
		genotype*treatment	1	0,005		0,947				
		Error	37							
	Base of Support (Hind paws)								Univariate GLM	Bonferroni
		genotype	1	0,052		0,820	−0,013	−0,125–0,100		
		treatment	1	4,324		0,045	0,115	0,227–0,003		
		genotype*treatment	1	1,151		0,290				
		Error	37							
	Stride length (Front Right)								Univariate GLM	Bonferroni
		genotype	1	5,509		0,024	0,495	0,068–0,923		
		treatment	1	1,885		0,178	0,290	−0,138–0,717		
		genotype*treatment	1	0,221		0,641				
		Error	37							
	Stride length (Front Left)								Univariate GLM	Bonferroni
		genotype	1	5,675		0,022	0,500	0,075–0,925		
		treatment	1	2,140		0,152	0,307	−0,118–0,732		
		genotype*treatment	1	0,006		0,937				
		Error	37							
	Stride length (Rear Right)								Univariate GLM	Bonferroni
		genotype	1	3,935		0,055	0,531	−0,011–1,074		
		treatment	1	1,107		0,300	0,282	−0,261–0,825		
		genotype*treatment	1	0,790		0,380				
		Error	37							
	Stride length (Rear Left)								Univariate GLM	Bonferroni
		genotype	1	3,224		0,080	0,483	−0,060–1,027		
		treatment	1	0,585		0,449	0,205	−0,338–0,749		
		genotype*treatment	1	0,092		0,763				
		Error	37							
	Max contact area (Front Right)								Univariate GLM	Bonferroni
		genotype	1	0,051		0,822	0,010	−0,076–0,095		
		treatment	1	0,089		0,767	−0,013	−0,098–0,073		
		genotype*treatment	1	0,008		0,929				
		Error	37							
	Max contact area (Front Left)								Univariate GLM	Bonferroni
		genotype	1	0,006		0,939	−0,003	−0,080–0,074		
		treatment	1	0,106		0,747	−0,012	−0,089–0,065		
		genotype*treatment	1	0,001		0,986				
		Error	37							
	Max contact area (Rear Right)								Univariate GLM	Bonferroni
		genotype	1	0,011		0,918	0,005	−0,090–0,100		
		treatment	1	0,544		0,465	−0,035	−0,130–0,061		
		genotype*treatment	1	0,126		0,724				
		Error	37							
										Bonferroni

(*continued on next page*)

Table 1 (*continued*)

Task	Variable	Source	df	F	Chi-Square	p-value	Mean difference	95% CI (difference)	Statistical Test	Adjustment
	Max contact area (Rear Left)								Univariate GLM	
		genotype	1	0,001		0,995	0,000	−0,094–0,094		
		treatment	1	0,344		0,561	−0,027	−0,121–0,067		
		genotype*treatment	1	0,022		0,918				
		Error	37							
	Dynamic Data Run Duration								Univariate GLM	Bonferroni
		genotype	1	0,151		0,699	−0,050	−0,312–0,212		
		treatment	1	0,001		0,977	−0,004	−0,266–0,258		
		genotype*treatment	1	0,043		0,837				
		Error	37							
	Step cycle (Front Right)								Univariate GLM	Bonferroni
		genotype	1	0,421		0,520	0,008	−0,017–0,033		
		treatment	1	1,101		0,301	0,013	−0,012–0,037		
		genotype*treatment	1	0,069		0,795				
		Error	37							
	Step cycle (Front Left)								Univariate GLM	Bonferroni
		genotype	1	0,099		0,755	0,004	−0,022–0,030		
		treatment	1	1,885		0,178	0,018	−0,008–0,044		
		genotype*treatment	1	0,550		0,463				
		Error	37							
	Step cycle (Rear Right)								Univariate GLM	Bonferroni
		genotype	1	0,820		0,371	0,010	−0,012–0,032		
		treatment	1	0,850		0,363	0,010	−0,012–0,032		
		genotype*treatment	1	0,049		0,826				
		Error	37							
	Step cycle (Rear Left)								Univariate GLM	Bonferroni
		genotype	1	0,390		0,536	0,006	−0,013–0,025		
		treatment	1	0,355		0,555				
		genotype*treatment	1	0,001		0,933				
		Error	37							
	Swing speed (Front Right)								Univariate GLM	Bonferroni
		genotype	1	0,006		0,940	0,219	−5,671–6,108		
		treatment	1	0,123		0,728	1,019	−4,870–6,909		
		genotype*treatment	1	0,037		0,849				
		Error	37							
	Swing speed (Front Left)								Univariate GLM	Bonferroni
		genotype	1	0,343		0,562	1,626	−4,000–7,252		
		treatment	1	0,285		0,597	1,483	−4,144–7,109		
		genotype*treatment	1	0,002		0,962				
		Error	37							
	Swing speed (Rear Right)								Univariate GLM	Bonferroni
		genotype	1	0,079		0,780	0,787	−4,872–6,446		
		treatment	1	0,001		0,989	−0,039	−5,697–5,620		
		genotype*treatment	1	0,123		0,728				
		Error	37							
	Swing speed (Rear Left)								Univariate GLM	Bonferroni
		genotype	1	0,137		0,713	−1,050	−6,798–4,698		
		treatment	1	0,127		0,723	−1,012	−6,760–4,736		
		genotype*treatment	1	0,241		0,626				
		Error	37							
RotaRod										
	Time spent on the rod								Univariate GLM	Bonferroni
		genotype	1	0,048		0,828	−5,123	−52,599–42,354		
		treatment	1	0,056		0,815	5,523	−41,954–52,999		
		genotype*treatment	1	1,345		0,254				
		Error	37							
	Number of rotations								Negative binomial	Bonferroni
		genotype	1		0,939	0,332				
		treatment	1		0,007	0,931				
		genotype*treatment	1		0,670	0,413				
									Linear Mixed Effect Model	Bonferroni

(*continued on next page*)

Table 1 (*continued*)

Task	Variable	Source	df	F	Chi-Square	p-value	Mean difference	95% CI (difference)	Statistical Test	Adjustment
Sensory Motor Gating		genotype		13,890		0,001	7,211	3,387–11,035		
		treatment		0,444		0,506	1,289	−2,536–5,113		
		genotype*treatment		3,656		0,058				
	Averaged Startle Force								Univariate GLM	Bonferroni
		genotype	1	4,274		0,046	7,174	0,143–14,204		
		treatment	1	0,143		0,708	1,131	−5,719–8,341		
		genotype*treatment	1	1,135		0,294				
		Error	37							
Open Field	Time in the center field								Univariate GLM	Bonferroni
		genotype	1	1,485		0,231	22,501	−14,918–59,920		
		treatment	1	0,181		0,673	7,866	−29,553–45,284		
		genotype*treatment	1	0,047		0,830				
		Error	37							
	Travelled distance								Univariate GLM	Bonferroni
		genotype	1	0,315		0,578	−343,435	−1583,965–897,096		
		treatment	1	1,791		0,189	−819,347	−2059,878–421,184		
		genotype*treatment	1	0,697		0,409				
		Error	37							
Morris Water Maze	ACQUISITION									
	Mean swim speed								Univariate GLM	Bonferroni
		genotype	1	0,040		0,842	0,145	−1,322–1,611		
		treatment	1	3,672		0,063	−1,387	−2,853–0,080		
		genotype*treatment	1	0,004		0,952				
		Error	37							
	Escape latency								Linear Mixed Effect Model	Bonferroni
		genotype		0,540		0,4632	1,466	−2,491–5,423		
		treatment		11,231		0,001	6,646	2,689–10,603		
		genotype*treatment		0,183		0,670				
	Escape path lenght								Linear Mixed Effect Model	Bonferroni
		genotype		0,119		0,730	13,178	−62,130–88,486		
		treatment		4,167		0,043	77,891	2,583–153,199		
		genotype*treatment		0,001		0,974				
	Thigmotaxis								Linear Mixed Effect Model	Bonferroni
		genotype		0,945		0,333	1,139	1,177–3,456		
		treatment		9,732		0,002	3,656	1,339–5,973		
		genotype*treatment		0,061		0,805				
	Mean distance to the platform								Linear Mixed Effect Model	Bonferroni
		genotype		0,095		0,759	0,281	−1,521–2,083		
		treatment		13,827		0,001	3,395	1,593–5,197		
		genotype*treatment		0,024		0,877				
	PROBE TRIAL (Day5)									
	Time spent in the platform zone (Day 5)								Univariate GLM	Bonferroni
		genotype	1	0,033		0,857	−0,24	−3,808–3,328		
		treatment	1	2,928		0,095	−2,188	−5,756–1,380		
		genotype*treatment	1	0,018		0,894				
		Error	37							
	N of crosses of platform zone (Day 5)								Negative binomial	Bonferroni
		genotype	1		0,009	0,927				
		treatment	1		0,403	0,526				
		genotype*treatment	1		0,002	0,965				
	Mean distance to the platform (Day 5)								Univariate GLM	Bonferroni
		genotype	1	0,321		0,575	1,609	−4,147–7,365		
		treatment	1	2,169		0,149	4,183	−1,573–9,940		
		genotype*treatment	1	0,068		0,796				
		Error	37							
	Mean swim speed (Day 5)								Univariate GLM	Bonferroni
		genotype	1	0,104		0,749	−0,301	−2,193–1,592		
		treatment	1	2,535		0,120	−1,487	−3,380–0,405		
		genotype*treatment	1	1,515		0,226				
		Error	37							
Passive Avoidance									Linear Mixed Effect Model	Bonferroni
		genotype		1,268		0,267	−3,544	−9,917–2,828		

(*continued on next page*)

Table 1 (*continued*)

Task	Variable	Source	df	F	Chi-Square	p-value	Mean difference	95% CI (difference)	Statistical Test	Adjustment
		treatment		0,686		0,413	2,607	−3,766–8,979		
		genotype*treatment		0,098		0,756				

genotypes, the induction of TBI resulted in a unilateral neocortical lesion, characterized by a developing cavity affecting the somatosensory cortices and cytoarchitectonic alterations in the septal hippocampus unilateral to the cavity (Supplementary Fig. 1). Using unfolded cortical maps, we defined the cortical areas affected by the brain injury (Fig. 1E) and calculated the lesion area. We observed comparable lesions in the two genotypes (WT-CCI: 12.17 ± 0.69 mm^2, TG-CCI: 10.91 ± 0.69 mm^2; $p = 0.26$) (Fig. 1F), which extend over the visual and the somatosensory cortices. The ex-vivo analysis of the lesion cavity confirmed that the brain pathology develops similarly in both genotypes (cortical volume loss, WT-CCI: 5.88 ± 1.45%, TG-CCI: 4.84 ± 1.45%; $p = 0.55$) (Fig. 1G).

Developmental lymphatic dysfunction affects acute neurological recovery but does not exacerbate chronic functional outcomes. We next examined the effect of pre-existing mLV dysfunction on the recovery of post-TBI behavioral impairment (Fig. 2A). Acute impairment of motor functions (Composite Neuroscore) was observed in both WT-CCI and TG-CCI mice, as measured at 2 dpi (genotype effect: $p = 0.82$, TBI effect: $p = 0.001$) (Fig. 2B and Supplementary Table 1). However, while in WT animals motor functions recovered at 7 dpi (WT-CCI: 85.3 ± 2.9% compared to baseline; $p = 0.47$), motor impairment persisted in TG animals for up to 10 dpi (TG-CCI: 87.7 ± 2.4%, $p = 0.01$; genotype effect: $p = 0.07$) (Fig. 2B). No statistical differences were observed between genotypes in SHAM mice.

Analyses of motor coordination and balance at 1-month post-TBI overall showed neither genotype (WT vs. TG) nor TBI (CCI vs. SHAM) effects or genotype/TBI interaction in all the analyzed parameters. Catwalk and Rotarod analyses are summarized in Fig. 2C–F and Supplementary Table 1. In Catwalk gait analysis, a significant genotype effect was observed on the stride length, with TG mice showing a longer stride. The stride length difference between the two genotypes reached significance for the front paws (LF: $p = 0.02$; RF: $p = 0.02$) (Fig. 2C and D), with a trend for the hind paws (Supplementary Table 1). A TBI-related difference was instead observed in the analysis of the base of support (BoS, the distance between the paws or the pair) of hind paws, which was narrower in both WT- and TG-CCI compared to the respective SHAM group (TBI effect: $p = 0.045$) (Fig. 2E). Notably, none of the gait parameters revealed any lateral asymmetry, although the lesion was unilateral. Analysis of Rotarod did not reveal TBI or genotype effect in the time spent on the rod (Fig. 2F and Supplementary Table 1), nor in the number of completed turns (Supplementary Table 1).

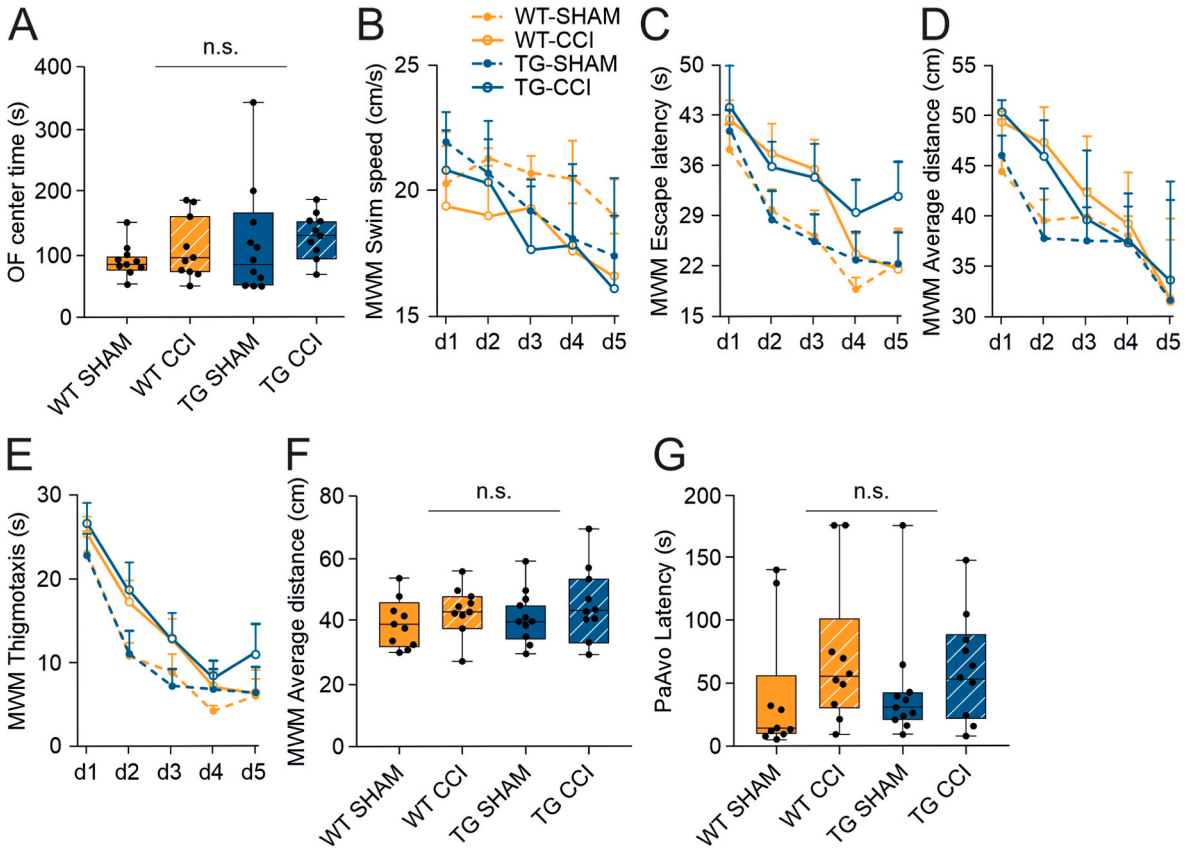

Fig. 3. Developmental mLV dysfunction does not exacerbate anxiety and learning-memory deficits in the early chronic phase post-TBI. (A) Open field task was used to evaluate anxiety in CCI and SHAM control mice. No genotype or injury differences were visible in the time spent in the center of the open field. (B–F) Learning and memory were assessed using the Morris swim task ('water maze'). The different parameters analyzed show a significant injury effect, but no differences between TG and WT mice. (B) Swimming speed; (C) Escape latency; (D) Average distance to the platform; (E) Wall-hugging (thigmotaxis); (F) Time spent in the platform zone on the probe trial (day 5). (G) No significant differences were observed in the passive avoidance task related to TBI induction or developmental deficits in the mLVs. Data analyses: linear mixed-effect model (lme) with Sidak correction. OF: open field, MWM: Morris water maze, PaAvo: passive avoidance. P-values are reported for the genotype effect analysis.

Sensory-motor gating (Fig. 2G) was tested by assessing the startle reflex in response to a sudden loud noise (110 dB), and the effects of pre-pulse inhibition at variable intensities (20, 35, and 50 dB). We observed a significant overall genotype difference in the startle force, with TG mice showing attenuated startles compared to WT controls ($p = 0.046$). On the other hand, increasing the intensity of the pre-pulse resulted in a comparable inhibition of the startle reflex in both genotypes (genotype effect at 20 dB: $p = 0.62$; at 35 dB: $p = 0.33$; at 50 dB: $p = 0.44$). This combination of results suggests that the TG mice generally have lower reactivity than their WT littermates. Still, the pre-pulse inhibition does not appear to be altered by the absence of mLVs. The body weight did not differ between the genotypes and thus cannot account for the observed differences (WT-SHAM: 29.9 ± 0.7; WT-CCI: 29.7 ± 0.7; TG-SHAM: 30.0 ± 0.7; TG-CCI: 31.0 ± 0.7; genotype effect: $p = 0.32$).

No differences between the genotypes were observed when testing TBI-related anxiety at week 3 post-injury (open field center time, genotype effect: $p = 0.23$; TBI effect: $p = 0.19$) (Fig. 3A and Supplementary Table 1). Similarly, the traversed distance in the open field did not differ between the experimental groups (genotype effect: $p = 0.58$; TBI effect: $p = 0.19$; Supplementary Table 1).

Morris swim task was used to test spatial learning and memory abilities at early-chronic time points. CCI mice presented slower learning in longer escape latency across the 5 acquisition days ($p = 0.001$) (Fig. 3C). Still, they also showed a tendency towards a slower swimming speed than SHAM controls ($p = 0.06$) (Fig. 3B and Supplementary Table 1).To rule out the contribution of swimming speed to impaired learning, we also analyzed other learning parameters that are not affected by swimming speed. We found that, independently from the genotype, CCI-mice kept a longer average distance to the platform (WT-SHAM: 38.49 ± 0.92 cm; WT-CCI: 41.74 ± 0.92 cm; TG-SHAM: 38.63 ±

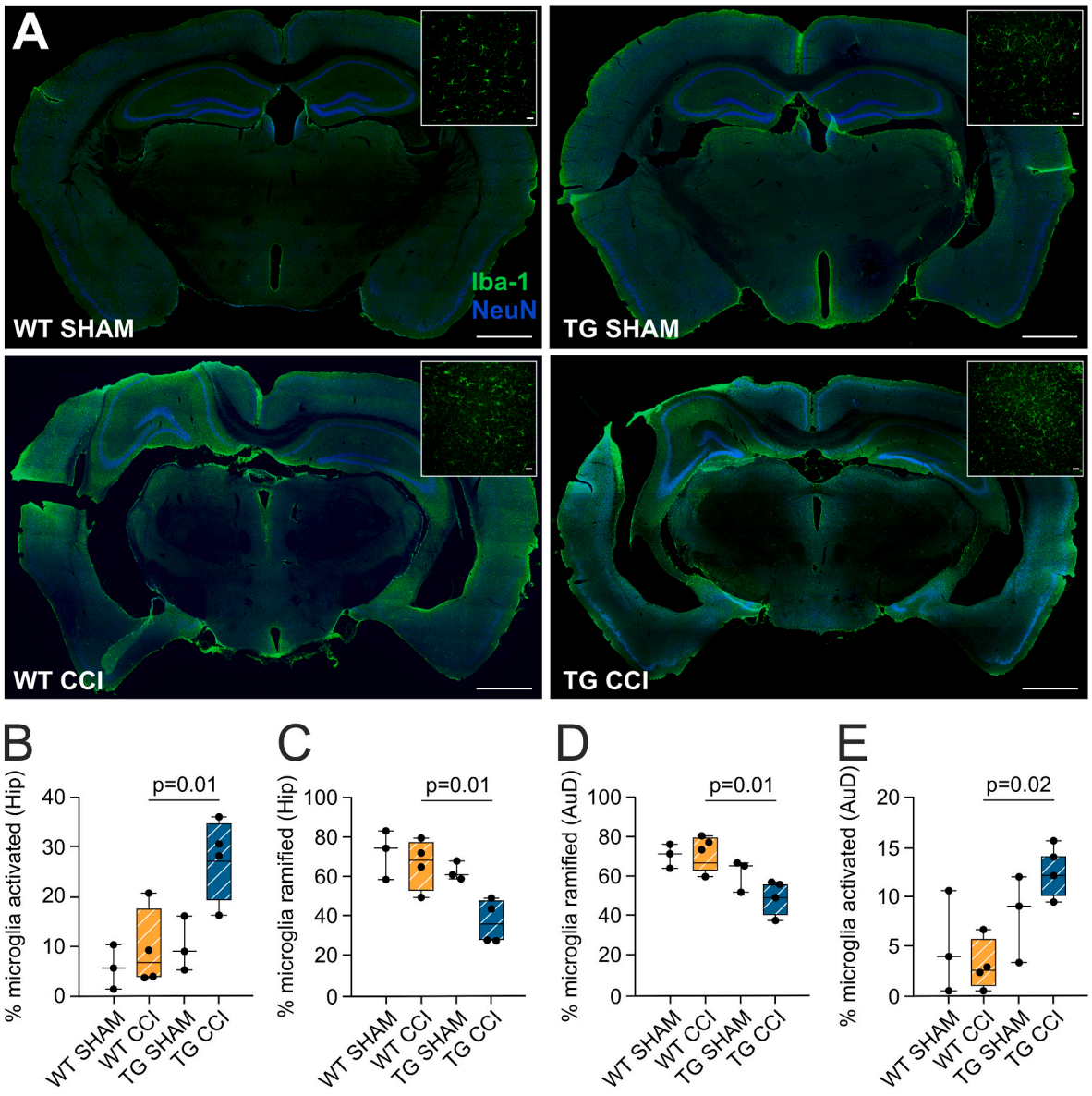

Fig. 4. Effect of developmental mLV dysfunction on TBI-related chronic microglia activation. (A) Representative photomicrographs (green; original magnification: × 10; scale bar = 1000 μm) showing Iba1-positive cells in cortical and subcortical areas of sham and CCI mice, 2 months post-TBI induction. Inserts in each panel show magnified microglial cells in representative areas of interest (original magnification, × 25; scale bar = 20 μm). (B, C) Quantitative analysis of number of Iba1-positive cells in the hippocampi (B) and in the auditory cortex (C) of WT-CCI and TG-CCI mice. (D) Quantitative analysis of percentage of ramified and activated microglia in the hippocampi of WT-CCI and TG-CCI mice. (E) Quantitative analysis of percentage of ramified and activated microglia in the auditory cortex of WT-CCI and TG-CCI mice. Data analyses: general linear model (GLM) with Sidak correction. (For interpretation of the references to colour in this figure legend, the reader is referred to the Web version of this article.)

0.88 cm; TG-CCI: 42.16 ± 0.92 cm; TBI effect: p = 0.001; Fig. 3D), spent more time close to the wall (thigmotaxis; WT-SHAM: 7.72 ± 1.19 s; WT-CCI: 11.09 ± 1.19 s; TG-SHAM: 8.57 ± 1.13 s; TG-CCI: 12.52 ± 1.19 s; TBI effect: p = 0.002) (Fig. 3E), and followed a longer path to reach the platform (WT-SHAM: 544.26 ± 38.60 cm; WT-CCI: 623.38 ± 38.60 cm; TG-SHAM: 558.66 ± 36.80 cm; TG-CCI: 635.33 ± 38.60 cm; TBI effect: p = 0.04). No genotype-related effect or interaction was observed (Supplementary Table 1). Hippocampal-dependent spatial memory was evaluated on a probe trial (day 5), by assessing the search bias in the pool after removing the platform. We found no difference between the groups in the time spent in the platform zone (TBI effect: p = 0.10; genotype effect: p = 0.86; Fig. 3F), in the number of crossings of the exact platform location, or the mean distance to the platform (Supplementary Table 1). These findings suggest that the search strategy but not the spatial memory is affected in CCI mice at an early chronic (i.e., first 2 months) phase post-TBI. The lack of mLVs does not affect the severity of learning and memory deficits.

We also employed the passive avoidance task to test a different form of long-term memory (fear conditioning). Here, the latency to enter the dark compartment was comparable in all experimental groups, independently from TBI or genotype (Fig. 3G and Supplementary Table 1), supporting the evidence that moderate TBI is not associated with memory impairment in this rodent model.

The lack of functional meningeal lymphatics impacts the post-TBI chronic neuroinflammatory adaptations. Neuroinflammation is a characteristic feature of post-TBI pathology (Owens et al., 2021; Janigro et al., 2020; Marchi et al., 2016). Increased neuroinflammation during the acute phase post-TBI has been associated with mLV downregulation (Bolte et al., 2020). Here, we specifically focused on microglia, reporting increased Iba1 immunoreactivity around the lesion (scar tissue), and in the proximal non-injured areas ipsilateral to the site of injury (Fig. 4A), in both WT-CCI and TG-CCI groups. Next, we analyzed the perilesional dorsal hippocampal formation (HPC) and auditory cortex (AuD), we found a significant TBI-related effect in HPC, with TBI mice showing more activated microglia than SHAM controls (TBI effect, HPC: p = 0.02; AuD: p = 0.61). In the HPC ipsilateral to the lesion, the percentage of activated microglia was significantly higher in the TG-CCI group (27.70 ± 8.40%) than in WT-CCI mice (9.44 ± 7.76%; p = 0.01), with the percentage of physiologically ramified microglia showing an opposite trend (Fig. 4B and C). The total number of microglial cells was similar in the two experimental groups. Similarly, in the perilesional AuD cortex, TG animals showed a significant increase in the percentage of activated microglia (TG-CCI: 12.42 ± 3.07%; WT-CCI: 2.99% ± 2.76%; p = 0.02), and a significant reduction of ramified ones (Fig. 4D and E). These data support the notion that impairments of mLV functionality can sustain a neuroinflammatory adaptation during the chronic phase of TBI pathology.

4. Discussion

Our data show that a congenital mLV dysfunction does not significantly exacerbate brain structural and behavioral modifications post-TBI. The microglial cells in the perilesional area are activated, possibly representing a lingering vulnerability element.

These results align with the notion that TBI represents a risk factor for life-long neurocognitive adaptations (Smith et al., 2013). Longitudinal studies demonstrated that the development of neurocognitive and behavioral disabilities after TBI is a dynamic process: while acute phases are characterized by the presence of intracerebral hemorrhage and edema development (Reifschneider et al., 2015), the neurodegenerative, neuroinflammatory, and cerebrovascular processes define the development of chronic TBI (McMillan et al., 2012), suggesting a transition of TBI into a secondary progressive disease.

Previous studies in experimental stroke and intracerebral hemorrhage models have demonstrated that ablation of mLVs aggravates cerebral hematoma and edema (Chen et al., 2020; Virenque et al., 2021), and increases infarct volume (Si et al., 2006). Our *in vivo* longitudinal analyses of hemorrhage and edema-related parameters did not show significant differences between TG mice and WT littermates post-TBI. In line with the anatomical findings, behavioral tests did not reveal an overall difference between TG and WT mice, although evidencing trauma-associated loss of functions both at acute and chronic phases. However, we identified a slower recovery of sensory-motor functions in the TG-CCI group. As meningeal lymphatics favor the circulation of immune cells and brain clearance (Aspelund et al., 2015; Louveau et al., 2018; Wojciechowski et al., 2021), the lack of mLVs could negatively impact the repair processes (Simon et al., 2017).

4.1. Does lymphatic function impact post-TBI sequelae?

Due to their anatomical localization, mLVs can be compromised due to the brain impact, both directly (by breaching during the injury) or indirectly (by compression as a consequence of cerebral swelling and increased intracranial pressure (Bolte et al., 2020)). It has been demonstrated that TBI causes temporary functional impairment of mLVs (Bolte et al., 2020): this disruption begins almost immediately and may take months to recover. It is conceivable that in WT-CCI mice, the mLV functionality is fully compromised after TBI induction, practically nullifying the pre-existing mLV deficit of the TG mice. Indeed, none of the analyzed functional or pathological outcomes revealed a difference related to the pre-existing lack of meningeal lymphatics.

Our data diverge from the previous evidence that lymphatic alterations underlie TBI-mediated cognitive dysfunction (Bolte et al., 2020). This outcome can be explained by the differences in the injury paradigms (location and severity of induced TBI), the models used to study mLV dysfunction (targeted pharmacologic photoablation of dorsal lymphatics (Bolte et al., 2020) *vs.* transgenic mice carrying developmental dysfunction), and the differences in the tasks and time of assessment of cognitive dysfunction. The location and severity of the injury directly affect the functional outcome. In the model used in our study, the induced impact involves most of the ipsilateral somatosensory cortex. It directly affects one of the previously shown hotspots essential for mLV drainage (Louveau et al., 2018), possibly leading to a prolonged post-TBI deficit in mLV drainage. Our conditions are more severe than the ones previously studied (Bolte et al., 2020). At the same time, the behavioral paradigms used to define cognitive dysfunctions, and the sensitivity of the used tasks (Frick et al., 2000), are different (novel location recognition test at 2 weeks post-TBI (Bolte et al., 2020) *vs.* Morris swim task and passive avoidance task at 6–8 weeks post-TBI), ultimately affecting the outcomes and representing a limitation. The different models used to study mLV functionality can also determine the deviations in the observed results. Indeed, our data suggest that developmental functional alterations of mLVs in the K14-VEGFR3-Ig TG mice are associated with changes in interstitial flow dynamics (Supplementary Fig. 2), resulting in the impairment of macromolecule drainage and clearance (Aspelund et al., 2015), which can exacerbate TBI pathology (Iliff et al., 2014). Finally, the effect of anesthesia during surgery on subsequent mLV dysfunction and behavioral analyses should be considered. The effect of anesthetic on interstitial fluid dynamics has been described (Benveniste et al., 2019; Hablitz et al., 2019), however its impact on meningeal lymphatic drainage remains an open question. Two recent works have provided insights by demonstrating that lymphatic vessels are affected by the use of anaesthetics and regulated by circadian rhythm (Hablitz et al., 2020; Ma et al., 2019). Similarly, our own data show an impact of anesthesia on mLV drainage (decreased CSF outflow) (Virenque et al., 2021): however, the anesthesia effect is temporary and the normal lymphatic function is restored within minutes. Therefore, it is conceivelable that the anesthesia *per se* would not have a long-term effect on mLV drainage and on the TBI-related functional or pathological outcomes.

4.2. Role of meningeal lymphatics on neuroinflammatory adaptations post-TBI

The development of TBI pathology in the CCI model has a dynamic profile, and behavioral deficits can appear beyond the timeframe considered in our behavioral study. Progression of functional damage can be delayed over several months, and cognitive abilities can degrade as a consequence of prolonged neuroinflammation (Di Sapia et al., 2021). Chronic inflammation induced by brain injuries can represent a player in developing neurodegenerative disorders, including dementia and CTE, and interventions aimed at attenuating neuroinflammation have proven successful in taming cognitive outcomes (Owens et al., 2021; Ichkova et al., 2020).

The meningeal lymphatic system is critical for modulating immune responses in the CNS, and pre-existing lymphatic dysfunction has been linked to the increase of TBI-mediated acute neuroinflammation (Bolte et al., 2020). Here, we expanded these findings, demonstrating that mLV dysfunction results in microglia morphological adaptations in the perilesional areas up to two months post-TBI. Although neuroinflammation is a characteristic feature of TBI, the persistence of inflammation correlates with the severity of the injury (Lagraoui et al., 2012). We report Iba1+ microglial morphological changes that suggest activation, specifically increased percentage of activated/ameboid and less physiological/ramified cells in CCI mice lacking the lymphatic system. These results are coherent with a transcriptomic analysis for this cell type reported before (Bolte et al., 2020). Altogether, this evidence supports the hypothesis of a pathological link between lymphatic functions and microglial cells in the setting of experimental head trauma. Our findings, therefore, suggest that pre-existing mLV deficits could represent a possible risk factor for the overall outcome of TBI pathology. In support of this hypothesis, we have recently reported an increased cytotoxic T cell response in the brain of K14-VEGFR3-Ig TG mice during the chronic phase of TBI pathology (Wojciechowski et al., 2021). The observed sustained neuroinflammation in TG-CCI mice could induce and support the activation of a T cell response, contributing to worsening the chronic TBI lesion (Wojciechowski et al., 2021; Daglas et al., 2019).

5. Conclusions

Overall, our data expand the knowledge on the role of meningeal lymphatics in the development and progression of TBI pathology. While pre-existing developmental defects in mLVs do not exacerbate the cortical lesion and the associated functional outcomes following brain injury, the disruptions in meningeal lymphatic function contribute to sustaining the chronic neuroinflammation and represent a susceptibility factor despite the lack of a functional phenotype. As neuroinflammation plays a pivotal role in the progression of TBI pathology, restoring or supporting mLV functionality after TBI could affect the overall chronic inflammatory processes and therefore represent a therapeutic opportunity for the prevention of secondary damages. Our data need to be validated in the clinical context to confirm the association between mLV dysfunction, neuroinflammation, and severity of the pathology, above all in the elderly population where a pre-existing deficit in the lymphatic vasculature are expected (Ahn et al., 2019; van Vliet and Marchi, 2022).

Author contributions

HT, NM, KA and FMN designed the experiments; AV, HK, SA, EZ, VA, ES, DM and AM performed the experiments; AV, HK, VA, ES, ER, NM, HT and FMN analyzed and interpreted data; AV, SA, TH, NM, KA and FMN wrote and revised the manuscript.

Declaration of competing interest

The authors declare no competing interests. The authors confirm they have read the Journal's position on issues involved in ethical publication and affirm that this report is consistent with those guidelines.

Acknowledgements

For their help with MRI sequences, the authors would like to thank Mikko Kettunen and Riikka Immonen (Biomedical Imaging Unit, National Bio-NMR facility) and Moataz Abdalkader, A.I.Virtanen Institute for Molecular Sciences, University of Eastern Finland. For the help in generating the unfolded cortical maps, we thank Ville Airaksinen, A.I. Virtanen Institute for Molecular Sciences, University of Eastern Finland. We also thank the Biomedicum Imaging Unit at the University of Helsinki for providing professional services and valuable help. We finally thank Academy Professor Asla Pitkänen (A.I.Virtanen Institute for Molecular Sciences, University of Eastern Finland) for the initial help in designing the study.

This work was supported by the Jane and Aatos Erkko Foundation (HT and KA), the Academy of Finland (grant 309479/2017 – FMN), The Sigrid Juselius Foundation (KA), European Research Council (ERC) under the European Union's Horizon 2020 research and innovation programme (grant 743155 – KA), and the Doctoral Program of Biomedicine (DPBM – AV and SA). This work was partially supported by Era-Net/ANR Neu-Vasc (NM) and Biocenter Finland (HK).

Appendix A. Supplementary data

Supplementary data to this article can be found online at https://doi.org/10.1016/j.bbih.2022.100466.

References

Ahn, J.H., et al., 2019. Meningeal lymphatic vessels at the skull base drain cerebrospinal fluid. Nature 572, 62–66.
Aspelund, A., et al., 2015. A dural lymphatic vascular system that drains brain interstitial fluid and macromolecules. J. Exp. Med. 212, 991–999.
Benveniste, H., Heerdt, P.M., Fontes, M., Rothman, D.L., Volkow, N.D., 2019. Glymphatic system function in relation to anesthesia and sleep states. Anesth. Analg. 128, 747–758.
Bolte, A.C., et al., 2020. Meningeal lymphatic dysfunction exacerbates traumatic brain injury pathogenesis. Nat. Commun. 11, 4524.
Chen, J., et al., 2020. Meningeal lymphatics clear erythrocytes that arise from subarachnoid hemorrhage. Nat. Commun. 11, 1–15.
Corps, K.N., Roth, T.L., McGavern, D.B., 2015. Inflammation and neuroprotection in traumatic brain injury. JAMA Neurol. 72, 355–362.
Daglas, M., et al., 2019. Activated CD8(+) T Cells cause long-term neurological impairment after traumatic brain injury in mice. Cell Rep. 29, 1178–1191 e6.
Ding, X.B., et al., 2021. Impaired meningeal lymphatic drainage in patients with idiopathic Parkinson's disease. Nat. Med. 27, 411–418.
Ekolle Ndode-Ekane, X., Kharatishvili, I., Pitkanen, A., 2017. Unfolded maps for quantitative analysis of cortical lesion location and extent after traumatic brain injury. J. Neurotrauma 34, 459–474.
Forner-Piquer, I., et al., 2021. Differential impact of dose-range glyphosate on locomotor behavior, neuronal activity, glio-cerebrovascular structures, and transcript regulations in zebrafish larvae. Chemosphere 267, 128986.
Franklin, K.B.J., Paxinos, G., 2007. The Mouse Brain in Stereotaxic Coordinates (Map). *Academic Press* (Academic Press (Elsevier).
Frick, K.M., Stillner, E.T., Berger-Sweeney, J., 2000. Mice are not little rats: species differences in a one-day water maze task. Neuroreport 11, 3461–3465.
Frieden, T. R., Houry, D. & Baldwin, G. Traumatic Brain Injury in the United States: Epidemiology and Rehabilitation.
Giannoni, P., et al., 2018. The pericyte–glia interface at the blood–brain barrier. Clin. Sci. 132, 361–374.
Hänninen, N., Rautiainen, J., Rieppo, L., Saarakkala, S., Nissi, M.J., 2017. Orientation anisotropy of quantitative MRI relaxation parameters in ordered tissue. Sci. Rep. 7.
Hablitz, L.M., et al., 2019. Increased glymphatic influx is correlated with high EEG delta power and low heart rate in mice under anesthesia. Sci. Adv. 5, eaav5447.
Hablitz, L.M., et al., 2020. Circadian control of brain glymphatic and lymphatic fluid flow. Nat. Commun. 11, 4411.
Hayward, N.M.E.A., et al., 2011. Magnetic resonance imaging of regional hemodynamic and cerebrovascular recovery after lateral fluid-percussion brain injury in rats. J. Cerebr. Blood Flow Metabol. 31, 166.
Holmin, S., Söderlund, J., Biberfeld, P., Mathiesen, T., 1998. Intracerebral inflammation after human brain contusion. Neurosurgery 42, 291–298.
Hu, X., et al., 2020. Meningeal lymphatic vessels regulate brain tumor drainage and immunity. Cell Res. 30, 229–243.

Ichkova, A., et al., 2020. Early cerebrovascular and long-term neurological modifications ensue following juvenile mild traumatic brain injury in male mice. Neurobiol. Dis. 141, 104952.
Iliff, J.J., et al., 2014. Impairment of glymphatic pathway function promotes tau pathology after traumatic brain injury. J. Neurosci. 34, 16180–16193.
Janigro, D., Kawata, K., Silverman, E., Marchi, N., Diaz-Arrastia, R., 2020. Is salivary S100B a biomarker of traumatic brain injury? A pilot study. Front. Neurol. 11, 528.
Janigro, D., et al., 2021. Peripheral blood and salivary biomarkers of blood–brain barrier permeability and neuronal damage: clinical and applied concepts. Front. Neurol. 11, 1767.
Konsman, J.-P., 2003. The mouse brain in stereotaxic coordinates. Psychoneuroendocrinology 28, 827–828.
Lagraoui, M., et al., 2012. Controlled cortical impact and craniotomy induce strikingly similar profiles of inflammatory gene expression, but with distinct kinetics. Front. Neurol. 3, 155.
Louveau, A., et al., 2015. Structural and functional features of central nervous system lymphatic vessels. Nature 523, 337–341.
Louveau, A., et al., 2018. CNS lymphatic drainage and neuroinflammation are regulated by meningeal lymphatic vasculature. Nat. Neurosci. 21, 1380–1391.
Mäkinen, T., et al., 2001. Inhibition of lymphangiogenesis with resulting lymphedema in transgenic mice expressing soluble VEGF receptor-3. Nat. Med. 7, 199–205.
Ma, Q., et al., 2019. Rapid lymphatic efflux limits cerebrospinal fluid flow to the brain. Acta Neuropathol. 137, 151–165.
Marchi, N., Banjara, M., Janigro, D., 2016. Blood-brain barrier, bulk flow, and interstitial clearance in epilepsy. J. Neurosci. Methods 260, 118–124.
McMillan, T.M., Teasdale, G.M., Stewart, E., 2012. Disability in young people and adults after head injury: 12-14 year follow-up of a prospective cohort. J. Neurol. Neurosurg. Psychiatry 83, 1086–1091.
Da Mesquita, S., Fu, Z., Kipnis, J., 2018a. The meningeal lymphatic system: a new player in neurophysiology. Neuron 100, 375–388.
Da Mesquita, S., et al., 2018b. Functional aspects of meningeal lymphatics in ageing and Alzheimer's disease. Nature 560, 185–191.
Mouzon, B.C., et al., 2014. Chronic neuropathological and neurobehavioral changes in a repetitive mild traumatic brain injury model. Ann. Neurol. 75, 241–254.
das Neves, S.P., Delivanoglou, N., Da Mesquita, S., 2021. CNS-draining meningeal lymphatic vasculature: roles, conundrums and future challenges. Front. Pharmacol. 12.
Noé, F.M., Marchi, N., 2019. Central nervous system lymphatic unit, immunity, and epilepsy: is there a link? Epilepsia Open 4, 30–39.
Owens, T.S., et al., 2021. Concussion history in rugby union players is associated with depressed cerebrovascular reactivity and cognition. Scand. J. Med. Sci. Sports 31, 2291–2299.
Patel, T.K., et al., 2019. Dural lymphatics regulate clearance of extracellular tau from the CNS. Mol. Neurodegener. 14, 11–19, 0312–x.
Reifschneider, K., Auble, B.A., Rose, S.R., 2015. Update of endocrine dysfunction following pediatric traumatic brain injury. J. Clin. Med. 4, 1536–1560.
Di Sapia, R., et al., 2021. In-depth characterization of a mouse model of post-traumatic epilepsy for biomarker and drug discovery. Acta Neuropathol. Commun. 9, 76.
Si, J., Chen, L., Xia, Z., 2006. Effects of cervical-lymphatic blockade on brain edema and infarction volume in cerebral ischemic rats. Chin. J. Physiol. 49, 258–265.
Simon, D.W., et al., 2017. The far-reaching scope of neuroinflammation after traumatic brain injury. Nat. Rev. Neurol. 13, 171–191.
Smith, D.H., Johnson, V.E., Stewart, W., 2013. Chronic neuropathologies of single and repetitive TBI: substrates of dementia? Nat. Rev. 9, 211–221.
Song, E., et al., 2020. VEGF-C-driven lymphatic drainage enables immunosurveillance of brain tumours. Nature 577, 689–694.
Tsai, H.-H., et al., 2022. Functional investigation of meningeal lymphatic system in experimental intracerebral hemorrhage. Stroke. https://doi.org/10.1161/STROKEAHA.121.037834.
Virenque, A., Balin, R., Noe, F.M., 2021. Title: dorsal skull meningeal lymphatic vessels drain blood-solutes after intracerebral hemorrhage. bioRxiv 3 (9), 434530. https://doi.org/10.1101/2021.03.09.434530, 2021.
van Vliet, E.A., Marchi, N., 2022. Neurovascular unit dysfunction as a mechanism of seizures and epilepsy during aging. Epilepsia. https://doi.org/10.1111/epi.17210.
Wojciechowski, S., et al., 2021. Developmental dysfunction of the central nervous system lymphatics modulates the adaptive neuro-immune response in the perilesional cortex in a mouse model of traumatic brain injury. Front. Immunol. 11, 559810.
Yanev, P., et al., 2020. Impaired meningeal lymphatic vessel development worsens stroke outcome. J. Cerebr. Blood Flow Metabol. 40, 263–275.
Zhao, S., Wang, X., Gao, X., Chen, J., 2018. Delayed and progressive damages to juvenile mice after moderate traumatic brain injury. Sci. Rep. 8, 7339.
Zou, W., et al., 2019. Blocking meningeal lymphatic drainage aggravates Parkinson's disease-like pathology in mice overexpressing mutated α-synuclein. Transl. Neurodegener. 8.